

RESEARCH ARTICLE

10.1002/2014JB011238

Key Points:

- Fully dynamic inversion able to retrieve the main features of the slip history
- Main motion for the 2004 Parkfield earthquake occurs in one elliptical region
- Only a small range of physical parameters gives rupture model explaining data

Supporting Information:

- Readme
- Text S1 and Figures S1–S6
- Figure S7
- Figure S8

Correspondence to:

C. Twardzik,
twardzik@eri.ucsb.edu

Citation:

Twardzik, C., S. Das, and R. Madariaga (2014), Inversion for the physical parameters that control the source dynamics of the 2004 Parkfield earthquake, *J. Geophys. Res. Solid Earth*, 119, doi:10.1002/2014JB011238.

Received 28 APR 2014

Accepted 7 AUG 2014

Accepted article online 12 AUG 2014

Inversion for the physical parameters that control the source dynamics of the 2004 Parkfield earthquake

C. Twardzik^{1,2}, S. Das¹, and R. Madariaga³

¹Department of Earth Sciences, University of Oxford, Oxford, UK, ²Now at Department of Earth Sciences, University of California, Santa Barbara, California, USA, ³Department of Geosciences, Ecole Normale Supérieure, Paris, France

Abstract A fully dynamic inversion for the earthquake source process, in which the geometry of the rupture area, the stress conditions, and frictional properties on the fault are obtained, is carried out by inverting displacement records for the 2004 M_w 6.0 Parkfield, California, earthquake. The rupture area of the earthquake is modeled using elliptical patches, and seismograms from 10 near-field digital stations are used. Synthetic tests to investigate the performance of the inversion in retrieving the rupture process demonstrate that we can reliably recover the large-scale features of the spatiotemporal distribution of slip. To investigate the stress conditions and frictional properties of the fault under which we produce a rupture model that fits the observed data, we explore the parameter space using a Monte Carlo method and find an optimal region where the source models fit the data well. The best fitting rupture process is shown to occur mainly within one horizontal elliptical region, 22 km long along strike and 4 km wide along depth. The seismic moment is 1.2×10^{18} N m, and the stress drop over the ellipse is ~ 4 MPa. The rupture speed, nearly constant during the entire rupture process, is ~ 2.9 km/s. The dimensionless quantity κ (roughly the strain energy change per unit fault surface divided by the energy release rate), which includes information on the stress and frictional properties on the fault, is found to be ~ 1.4 for the ellipse and strongly controls the rupture process along with the size of the initial circular patch that initiates the earthquake.

1. Introduction

The study of the earthquake source process requires rupture models that can be used to represent the earthquake. This can be approached in two different ways. One is by obtaining a kinematic rupture model, in which the slip history on the fault is determined by inverting seismograms but without reference to the forces causing the motion. Such a rupture process therefore provides the space-time distribution of source parameters such as the slip, slip rate, slip duration, and the rupture speed on the fault. The second one, the one we are interested in this study, is the dynamic rupture model, in which in addition to the above quantities, we also obtain the stress conditions and frictional properties on the fault, i.e., the constitutive law describing the behavior of the fault while it undergoes rupture.

The first attempt at dynamic inversion goes back to *Quin* [1990], in which a trial and error approach is used to infer the stress conditions on the fault for the M_w 6.4 1979 Imperial Valley earthquake, producing a dynamic rupture model compatible with the kinematic rupture model of *Archuleta* [1984]. Later, *Fukuyama and Mikumo* [1993] developed a joint kinematic/dynamic inversion for the rupture process of the M_{jma} 6.5 1990 Izu-Oshima, Japan, earthquake. They initially calculate the spatial and temporal pattern of slip from a spontaneous 3-D dynamic crack using the finite difference technique of *Mikumo et al.* [1987]. For this, they assumed that the fault is under a uniform shear stress load and has homogeneous strength. Then, using the source-time functions calculated from that initial dynamic rupture model, they perform a waveform inversion to obtain the spatiotemporal distribution of slip using the method of *Fukuyama* [1991]. Once this is obtained, an estimation of the stress drop and strength excess distribution on the fault is attempted, such that the spatial and temporal pattern of slip obtained by the dynamic modeling of the rupture is in agreement with the rupture model obtained by the waveform inversion. This estimation of the stress drop and strength excess is again based on the trial and error method used by *Quin* [1990]. The source-time functions obtained from that new dynamic rupture model are then fed back into the waveform inversion scheme before performing a new waveform inversion for the spatiotemporal distribution of slip. This is then done for a certain number of iterations until a satisfactory residual between observed and calculated waveforms is obtained.

The most common approach to estimate dynamic parameters consists of converting kinematic parameters, like slip distribution and rupture time, into dynamic parameters, such as static and dynamic stress distributions. *Ide and Takeo* [1997] introduced a statistical approach to objectively determine the stress conditions on the fault prior the rupture. Along the same lines, *Pulido and Irikura* [2000] developed a method to estimate parameters of the friction law from the inferred kinematic parameters, followed by many other studies [e.g., *Mikumo et al.*, 2003; *Fukuyama and Mikumo*, 2007; *Cruz-Atienza et al.*, 2009]. The inference of dynamic parameters from kinematic rupture models is still an active research topic [e.g., *Causse et al.*, 2014]. Our approach is different; we look directly for the friction law by inverting near-field observations.

Peyrat and Olsen [2004] were the first to develop a nonlinear dynamic inversion to study the rupture process of the M_w 6.8 2000 Tottori earthquake in which the stress drop and strength distributions, as well as the parameters of the constitutive law, are treated as unknowns. However, their use of a chessboard discretization introduced a large number of unknowns to be inverted for, as well as some mathematical issues with the stress discontinuities across the edges of each element. Following the approach developed by *Vallée and Bouchon* [2004] for kinematic inversion, *Di Carli et al.* [2010] resolved these issues by introducing elliptical subfaults during dynamic inversion. Recently, *Ruiz and Madariaga* [2011, 2013] combined the dynamic inversion with a Monte Carlo exploration of the parameter space to investigate the large nonuniqueness associated with dynamic inversion (e.g., as discussed by *Peyrat et al.* [2001]).

In this paper, we further develop this idea by performing a fully dynamic inversion for the source process of the 2004 Parkfield earthquake. Static, kinematic, and dynamic solutions for this earthquake have been obtained by different groups. For instance, *Murray and Langbein* [2006], *Johanson et al.* [2006], and *Barnhart and Lohman* [2010] have retrieved the static slip distribution from geodetic data. Some authors [e.g., *Bennington et al.*, 2011; *Ziv*, 2012] have used aftershocks distribution as constraints on their inversions of geodetic data. *Liu et al.* [2006] and *Ma et al.* [2008] have obtained a kinematic and dynamic rupture process using near-field strong-ground motion data. A kinematic source model using near-field strong motion has also been obtained by *Twardzik et al.* [2012]. Using regional seismic data, *Mendoza and Hartzell* [2008] have obtained a kinematic rupture history from P_{nl} waveforms. *Custodio et al.* [2009] and *Kim and Dreger* [2008] have carried out kinematic inversions using near-field strong-ground motion and geodetic data. More recently, *Houlié et al.* [2013] have computed a kinematic coseismic rupture history using 1 Hz GPS data. The comparison of the solutions (see Figure 1) shows overall consistency between the slip distributions retrieved by these different approaches. In particular, the rupture starts toward the southeastern end of the fault with some small slip near the hypocenter but the main slip area in every case is located about 20 km to the northwest of it, in a ~ 20 km² region. This is in contrast to earthquakes such as the 1992 M_w 7.2 Landers, California, earthquake [e.g., *Wald and Heaton*, 1994; *Cohee and Beroza*, 1994; *Cotton and Campillo*, 1995; *Hernandez et al.*, 1999] or the 1999 M_w 7.6 Izmit, Turkey, earthquake [e.g., *Yagi and Kikuchi*, 2000; *Delouis et al.*, 2002; *Sekiguchi and Iwata*, 2002; *Bouchon et al.*, 2002] in which different kinds of data (e.g., InSAR, GPS, teleseismic, and strong-ground motion data) led to inconsistent results. Other earthquakes present consistent kinematic inversions similar to what is observed for Parkfield, like, e.g., the 1995 M_w 6.8 Kobe, Japan, earthquake [*Ide and Takeo*, 1997; *Koketsu et al.*, 1998; *Bouchon et al.*, 1998] or more recently [*Guo et al.*, 2013]. Because of the very good quality data available in 2004, we think that the 2004 Parkfield earthquake is ideal for attempting a fully dynamic inversion.

The present paper is organized as follows. In section 2, we describe the data set and the methodology that we follow to carry out the inversion. We then perform synthetic tests in order to better understand our inversion technique (section 3). In section 4, we describe the results that we have obtained on the source process of the Parkfield earthquake from the fully dynamic inversion. Finally, in section 5, we present the results of the Monte Carlo exploration of the parameter space and summarize the conclusions in section 6.

2. Data Set and Methods

To determine the dynamic rupture process, we use three-component ~ 18 s long displacement waveforms, sampled at 0.035 s from 10 digital stations of the General Earthquake Observation System (GEOS) network [*Borcherdt et al.*, 1985]. This data set is the same as the one used by *Twardzik et al.* [2012] for kinematic inversions (see Figure 2). There were also 33 analog stations of the California Geological Survey (CGS) network that recorded the earthquake. We could not use them for dynamic inversion because these are triggered instrument that could have therefore missed the first arrivals. A flowchart showing all the steps in the

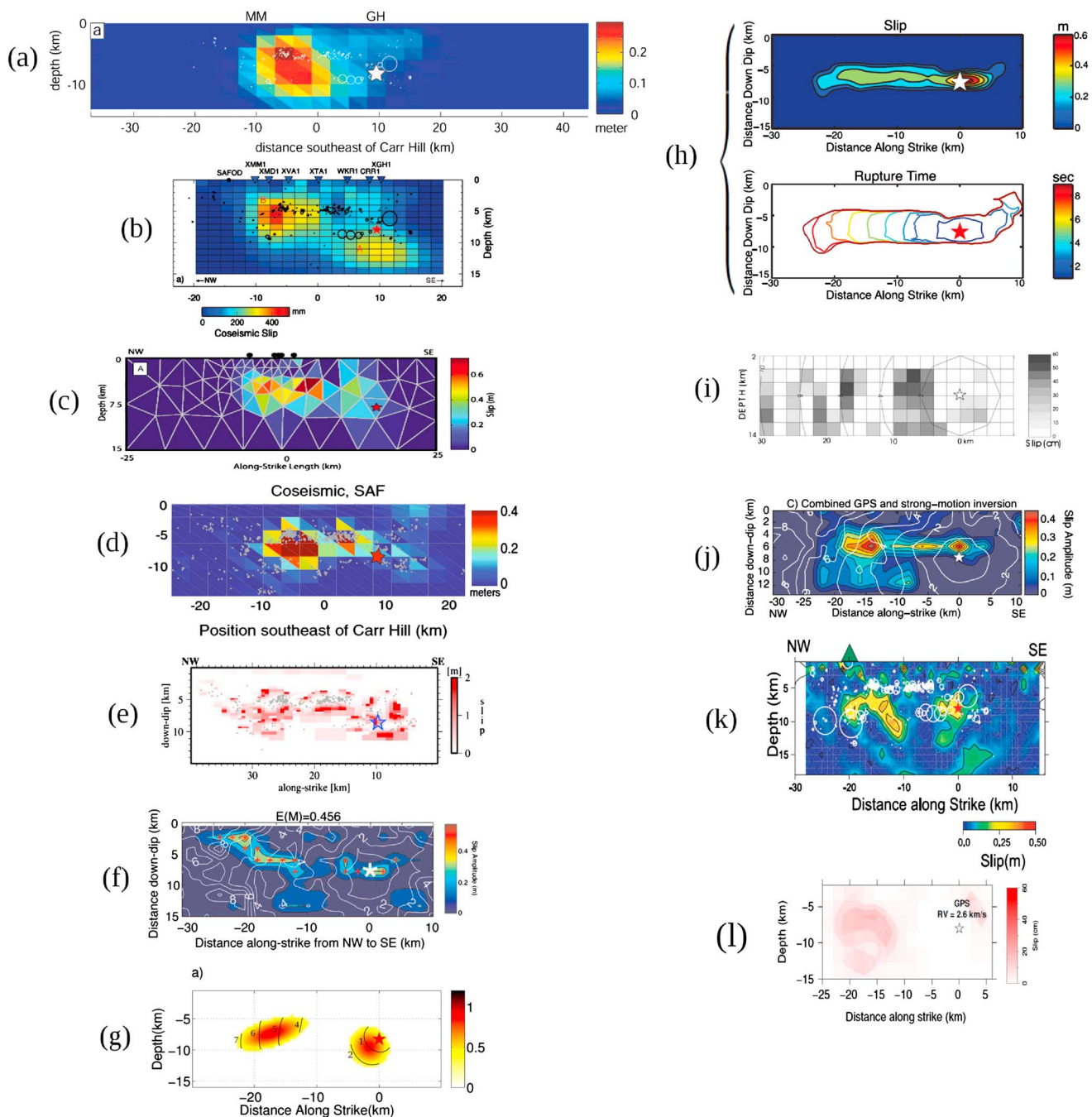


Figure 1. Solutions obtained from other studies for the slip distribution or rupture process of the 2004 Parkfield earthquake. (a) Murray and Langbein [2006] using GPS data. (b) Johanson et al. [2006] using InSAR and GPS data. (c) Barnhart and Lohman [2010] using GPS data. (d) Ziv [2012] using GPS data and aftershocks. (e) Bennington et al. [2011] using GPS data and aftershocks. (f) Liu et al. [2006] using strong-motion data. (g) Twardzik et al. [2012] using strong-motion data. (h) Ma et al. [2008] using strong-motion data. (i) Mendoza and Hartzell [2008] using regional P_{n1} waveforms. (j) Custodio et al. [2009] using strong-motion and GPS data. (k) Kim and Dreger [2008] using strong-motion, GPS, and InSAR data. (l) Houlié et al. [2013] using 1 Hz GPS data. Note that all figures have been rescaled to have the same spatial scale and are aligned with respect to the hypocenter (star). The left side of each rectangle is at the northwestern part of the fault (Figure 2).

dynamic inversion process is given in Figure 3. The forward modeling step of the flowchart consists of a full spontaneous rupture propagation in a 3-D medium on a pure right lateral strike-slip fault of 40 km long and 16 km depth, with a strike of 140° and a dip of 87° . The velocity structure adopted for the forward simulation is a 1-D structure corresponding to the northeast side of the San Andreas Fault. It is taken from Liu et al. [2006], itself determined by interpolation of the 3-D velocity structure of Thurber et al. [2003]. The propagation of the rupture is solved using a fourth-order staggered-grid finite difference method

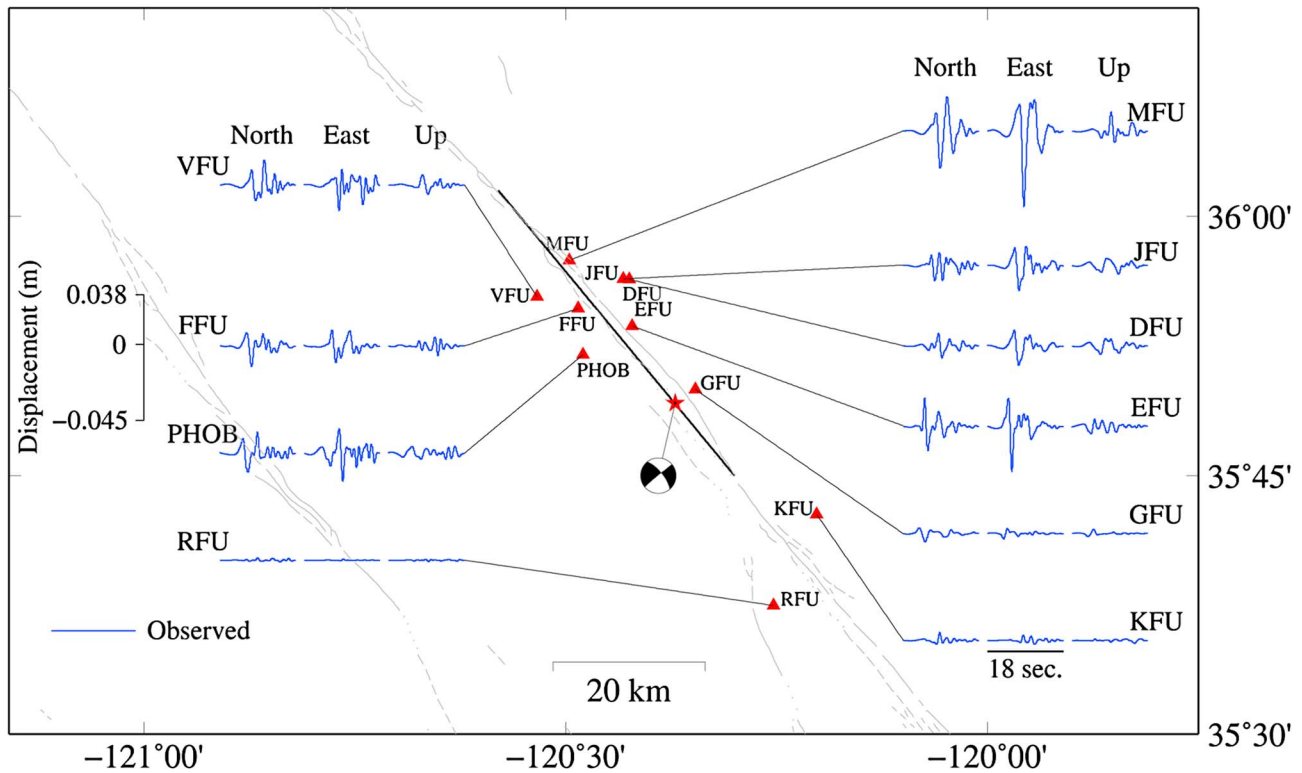


Figure 2. Tectonic setting, station distribution, and displacement seismograms used to study the 28 September 2004, M_w 6.0 Parkfield, California, earthquake. The stations are digital accelerometers from the GEOS network [Borcherdt et al., 1985] and are shown as red triangles. The original acceleration records are integrated twice into displacement records and filtered between 0.16 and 1.00 Hz using a fourth-order Butterworth filter. The filter is applied both in the forward and backward directions to obtain a zero-phase shift at all frequencies. The fault trace used during the inversion is shown by the thick black line. In grey, we show the surface expression of the faults in that region (fault traces from Jennings [1994]). The double-couple moment tensor from the Global Centroid Moment Tensor (GCMT) catalog is shown connected to the epicenter (red star). Note that each displacement seismogram starts at the origin time of the earthquake.

[Madariaga et al., 1998]. We use a spatial grid size of 250 m and a time step of 8.75×10^{-3} s, which is one fourth of the sampling rate of the displacement records. The Courant-Friedrichs-Lewy criterion for these values is 0.217, which ensures the stability of the numerical scheme [Madariaga et al., 1998]. Each forward simulation runs for 1280 time steps (i.e., equivalent to 11.2 s). The finite difference scheme includes a flat-free surface boundary condition at the top and Clayton-Engquist absorbing boundary conditions at the edges [Clayton and Engquist, 1977].

The fault was implemented by the thin-boundary conditions of Madariaga et al. [1998] (see Dalguer and Day [2007] for discussion about the use of these types of conditions). It is treated as an internal boundary on which we postulate that the rupture propagation is controlled by the slip-weakening friction law of Ida [1972]:

$$T(D) = (T_u - T_f) \left(1 - \frac{D}{D_c}\right) + T_f \quad \text{for } 0 < D < D_c, \quad (1)$$

$$T(D) = T_f \quad \text{for } D_c \leq D. \quad (2)$$

where T is the friction on the fault as a function of slip (D), T_u is the upper yield stress, T_f is the residual stress, and D_c is the characteristic slip-weakening distance. Because T_f cannot be determined from seismic observation alone [Madariaga, 1979], we set it to zero. Prior to the rupture, we assume that the fault is under an initial stress load (T_0), constant over the entire fault. The rupture area is defined by the distribution of T_u , describing the resistance of the fault to the propagation of the rupture. To generate this distribution, we use elliptical patches derived from the approach initially suggested by Vallée and Bouchon [2004] and

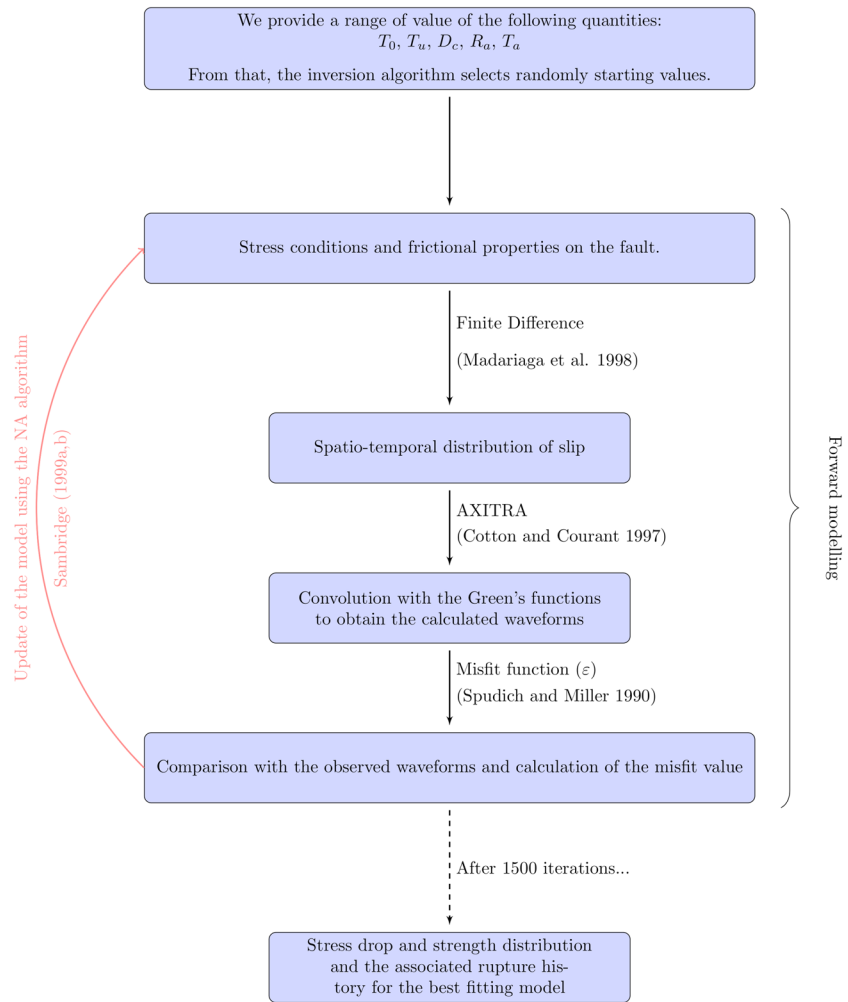


Figure 3. Flowchart of our dynamic inversion procedure.

widely used for dynamic inversion by *Di Carli et al.* [2010] and *Ruiz and Madariaga* [2011, 2013]. We use the parameter S , originally defined by *Hamano* [1974] as

$$S = (T_u - T_0) / (T_0 - T_f) \tag{3}$$

where, as mentioned above, $T_f = 0$. *Di Carli et al.* [2010] and *Ruiz and Madariaga* [2011, 2013] invert for T_u and T_0 separately, which occasionally leads to $T_0 > T_u$. To avoid this, we invert for S and T_0 (deducing T_u from it). In our study, we also modified the approach used in these studies, where S is assumed to be constant inside an ellipse, by taking an elliptical distribution of S inside each ellipse:

$$S(x, y) = S_{\max} \left(1 - \left(\frac{x^2}{a^2} + \frac{y^2}{b^2} \right) \right) \tag{4}$$

where S_{\max} is the maximum value of S allowed inside the ellipse and (x, y) represent the location of a point relative to the center such as $x = y = 0$ at the center of the ellipse. This modification aims to mimic the concept introduced by *Das and Kostrov* [1983] in which the edge of a patch is weaker than its center. In the inversions, we assumed that D_c had a constant value over the whole fault. This is necessary to obtain a uniform resolution in the finite difference simulations. In addition, *Guatteri and Spudich* [2000] and *Peyrat et al.* [2004] have argued that the energy release rate ($G_c = \frac{1}{2} T_u D_c$) is the most reliable quantity that can be determined by dynamic inversion. Therefore, varying T_u inside each ellipse is sufficient to obtain different values of G_c for each ellipse. To ensure that the rupture does not propagate outside the ellipse, we assume that the region outside has a positive and large upper yield stress (T_{out}), 10 times $T_{u_{\max}}$, where $T_{u_{\max}}$ is the maximum value of T_u encountered inside the entire rupture area. In order to trigger the rupture, we use a small

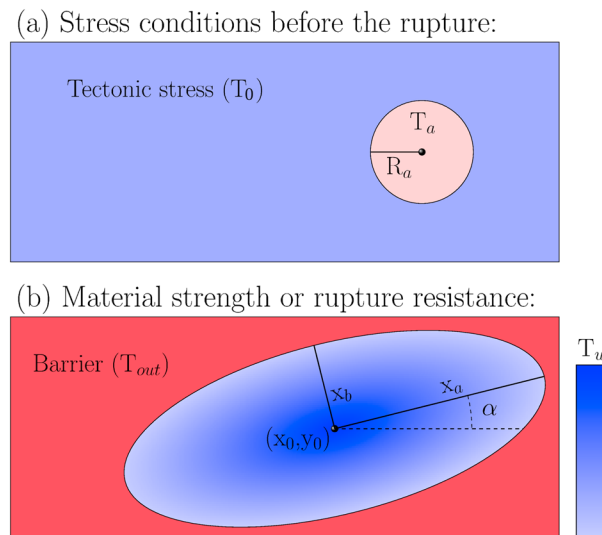


Figure 4. (a) Stress conditions before the spontaneous rupture propagation. The fault is loaded at a constant stress T_0 , and there is an initial circular patch at the hypocenter of radius R_a and strength T_a . Note that we assume a constant slip-weakening distance D_c over the entire fault. (b) Distribution of the material strength on the fault. The area where the rupture can occur is defined by elliptical patches, each having a geometry defined by five parameters: (x_0, y_0) that locate the center of the ellipse on the fault plane; (x_a, x_b) that are the length of the semimajor and semiminor axes, respectively; α that is the dip angle of the ellipse relative to the flat horizontal surface. Inside the ellipse, the material strength (T_u) is defined by an elliptical distribution centered at (x_0, y_0) . Outside the ellipse, we have a region of very high rupture resistance (T_{out}).

patch of radius R_a and strength T_a located at the hypocenter. To make sure that the rupture is always ready to propagate, we defined T_a as

$$T_a = \alpha T_{u_{max}} \quad (5)$$

where α is a factor that is always assumed to be ≥ 1 .

In order to obtain reasonable computation time, we do not propagate the waves emitted by the fault to each receiver using the finite difference method. Instead, we calculate the three-component displacement records at each station by convolving the obtained slip rate history on the fault with the Green's functions calculated using AXITRA, developed by Cotton and Coutant [1997]. This approach has the obvious limitation that AXITRA can only compute Green's functions for a 1-D velocity structure. AXITRA also uses a large amount of computer memory as the fault becomes bigger. For this reason, there is an upper bound on the size of the earthquake that can be studied in a reasonable computer time. Currently, above M_w 7.5 the inversion becomes too

expensive which therefore gives to the M_w 6.0 Parkfield earthquake an additional advantage for using the methods proposed in this study. The inversions performed in this study take about 278 h (~11 days) on 32, 2.6 GHz, CPUs and require at least 20 GB of memory.

The inversion is carried out using the Neighborhood Algorithm developed by Sambridge [1999a, 1999b]. It performs a direct search of the optimal solution inside the parameter space using Voronoi cells. At each iteration, the algorithm divides the parameter space into a set of n_s Voronoi cells, one for each rupture model. Geometrically, one Voronoi cell is a polyhedron that encloses a region of the parameter space containing models that have produced waveforms fitting similarly the data. The misfit between the calculated

Table 1. Description of the Parameters Used During the Inversion

For Each Ellipse	Description
x_0	Position along strike of the center of the ellipse
y_0	Position along dip of the center of the ellipse
x_a	Length of the semimajor axis
x_b	Length of the semiminor axis
ϕ	Dip of the semimajor axis with respect to the horizontal fault surface
S	Maximum value of the parameter S , located at the center of the ellipse and used to calculate the elliptical distribution of S inside the ellipse
For the Fault Plane	
T_0	Background stress of the fault prior initiation of the rupture
R_a	Size of the initial circular patch required to initiate the rupture at the hypocenter
α	Parameter that is used to determine the strength (T_a) of the initial circular patch: $T_a = \alpha T_{u_{max}}$
D_c	Characteristic slip-weakening distance

waveforms and the observed waveforms is measured through the following cost function proposed by *Spudich and Miller* [1990]:

$$\epsilon = \sum_{i=1}^{N_d} W_i \left(\frac{\sum_{t_b}^{t_e} (u_i^o(t) - u_i^c(t))^2}{\sum_{t_b}^{t_e} u_i^o(t)^2 + \sum_{t_b}^{t_e} u_i^c(t)^2} \right) \quad (6)$$

In this equation, $u_i^o(t)$ are the observed waveforms and $u_i^c(t)$ are the calculated waveforms. W_i refers to the weight given at each station and for each component, with value chosen according *Liu et al.* [2008]. N_d is the number of records and (t_b, t_e) gives the beginning and end times of the displacement records. Once an iteration is done, a new set of n_s models is resampled, for the next iteration, within the Voronoi cells that contain the n_r lowest misfit models. For the inversion, we use $n_s = 32$ and $n_r = 8$ and carry on the iterative process for 1500 iterations.

To summarize (Figure 4 and Table 1), we invert for the location and size of two elliptical patches (five parameters per ellipse) and the distribution of S inside these ellipses, determined using the value of S_{\max} for each one. We use two ellipses to model the rupture area in order to keep the number of parameters sufficiently low during the inversion; two ellipses are also in agreement with the study of the Parkfield earthquake by *Twardzik et al.* [2012], who performed kinematic inversion using elliptical patches. In that paper we discussed how to choose the number of ellipses when a new earthquake is being investigated. In addition to these 12 geometrical parameters, we invert for the initial stress load of the fault (T_0) as well as the size R_0 and strength T_a of the initial circular patch located at the hypocenter. T_a is determined from the factor α (equation (5)). Finally, we invert for the characteristic slip-weakening distance (D_c) in order to have a full description of the friction law and thus have 16 parameters that we attempt to invert for.

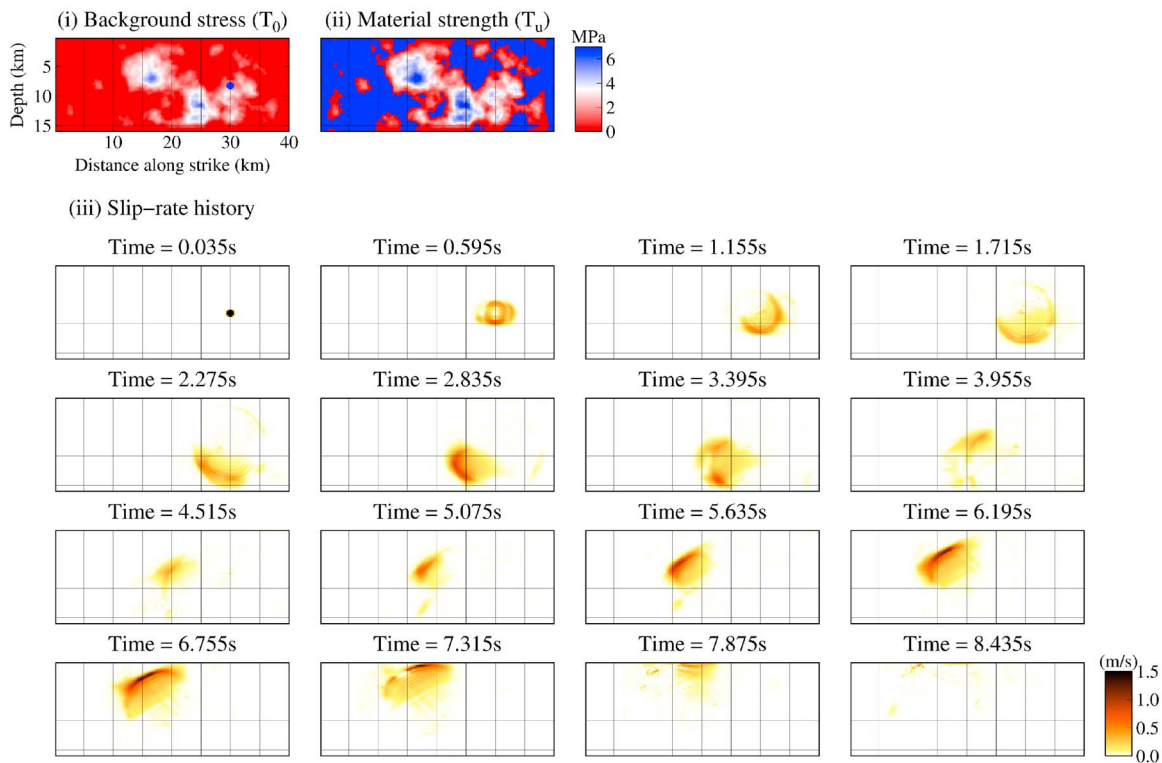
3. Synthetic Tests

To investigate the performance of this dynamic inversion technique, which uses ellipses to parameterize the rupture area, we perform synthetic tests. For this, we generate three-component synthetic displacement data filtered between 0.16 and 1.00 Hz at the 10 digital stations shown in Figure 2. The artificially created earthquake, used to generate the synthetic displacement data, occurs on the same fault as that used during the inversion, also shown in Figure 2. It is important to note that the slip history of the artificially created earthquake is not based on an elliptical parameterization of the rupture area. It is constructed using a k^{-2} -type slip distribution following the method of *Ruiz et al.* [2007]. From that slip distribution, we calculate the static stress drop (T_0) using the method of *Ripperger and Mai* [2004]. We then determine the material strength using a constant S value over the entire fault of 0.3. Wherever the fault experiences a positive static stress change from the initial slip distribution is considered as a barrier, and the barrier is constructed by forcing S to be very large ($S \gg 1.0$) in those regions. For the friction law, we use a constant D_c of 0.2 m. With those stress conditions, we calculate the rupture history and the synthetic displacement data using the methodology presented in the previous section. To trigger the earthquake, we use an initial circular patch located at the hypocenter with a radius of 0.63 km and a strength of 20 MPa.

Figure 5a shows the stress conditions prior to the rupture and snapshots of the slip history for the artificially created earthquake. The seismic moment is about 2.3×10^{18} N m. The rupture first propagates downward and along strike, reaching the bottom of the fault after 3.395 s and giving a rupture speed of about 2.5 km/s. It then moves upward and further along strike, breaking the region of largest slip after 6.755 s, resulting in a small increase of the rupture speed to ~ 3.15 km/s. After that, a small region near the surface, in the backward direction relative to the main area of slip, breaks after 7.315 s and ends the rupture. The fully dynamic inversion for the rupture process of the artificially created earthquake reaches a misfit value of 0.07, which is small enough that no differences are visible between the synthetic displacement data and the calculated waveforms from the lowest misfit rupture model.

Figure 5b shows the stress conditions prior the rupture and snapshots of the slip history for the lowest misfit rupture model. The tectonic stress found by the dynamic inversion is about 2 MPa. Because we assume a constant T_0 over the entire fault, the inversion does not recover any of the variability observed for the artificially created earthquake. Instead, it has found a value that is approximately equal to the average value of the tectonic stress of the artificially created earthquake (~ 1 MPa). For the material strength, we observe that the location of the ellipses is such that they overlap with the regions of high T_u , recovering relatively well

(a) Artificially Created Earthquake:



(b) Lowest Misfit Rupture Model:

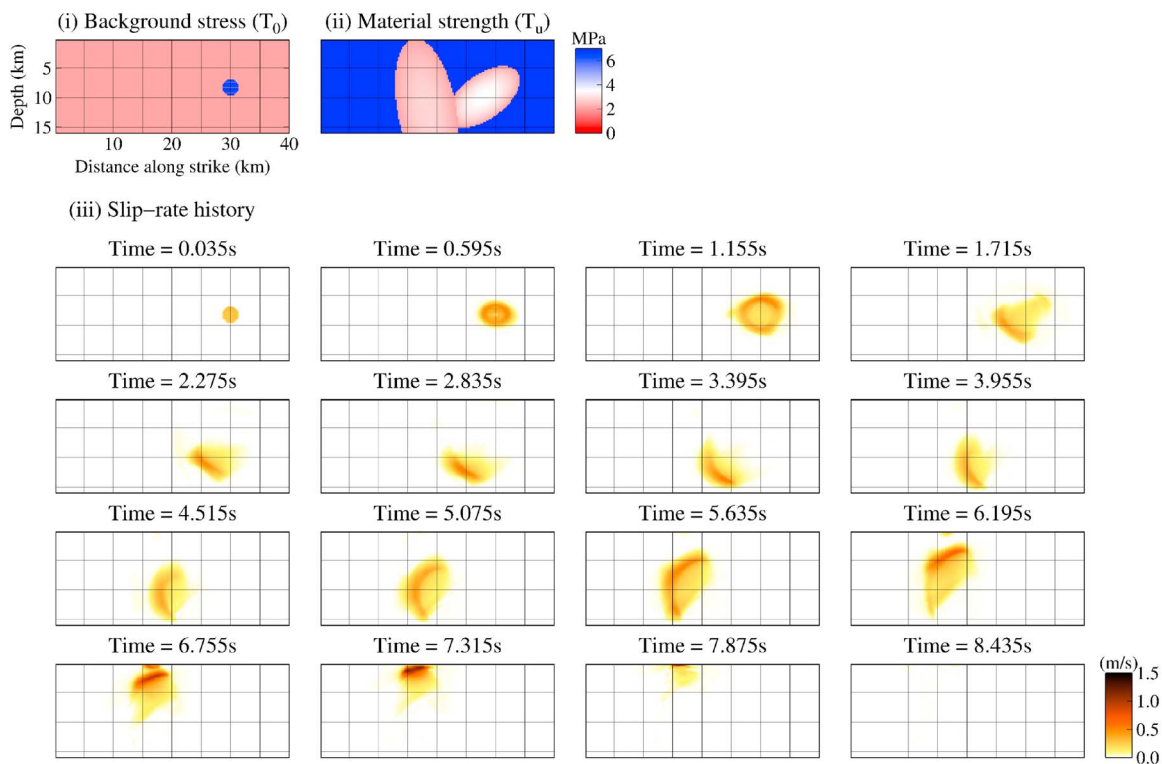


Figure 5. (a) Artificially created earthquake: Initial distribution of stress and strength on the fault prior to rupture (i and ii) and snapshots of the slip history every 0.56 s (iii) used to generate the synthetic seismograms. (b) Lowest misfit rupture model: Initial distribution of stress obtained on the fault prior to rupture (i and ii) and snapshots of the recovered slip history every 0.56 s (iii).

the rupture area of the artificially created earthquake. The maximum S value for the ellipse connected to the hypocenter is about 0.6, while it is 0.3 for the second ellipse. The low amplitude of the material strength compared to the artificially created earthquake is consequently caused by the underestimation of T_0 , since the S values found by the inversion are either greater than or equal to the value used for the artificially created earthquake. However, we will show in section 5 that the dynamic inversion does not perform well in reliably constraining S . The value of D_c (0.2 m) is recovered almost perfectly by the inversion, while the size (1.3 km) and strength (11.8 MPa) of the initial circular patch differ from the values used for the artificially created earthquake. However, the increase of the size of the initial circular patch by a factor of 2 is accompanied with a decrease of the strength by a factor of 2 so that both patches are similar in term of energy balance.

As a result of these stress conditions, the rupture model reaches a seismic moment of 2.3×10^{18} N m, which is the same as that of the artificially created earthquake. Regarding the slip history, we observe a similar process between the artificially created earthquake and that obtained by the dynamic inversion. We first have a downward and along-strike progression of the rupture, reaching the bottom of the fault at about 3.395 s, followed by upward and along-strike propagation, reaching the 5 km depth level at ~ 5.635 s. Until this time, the slip history is almost the same as that of the artificially created earthquake, after which we start observing some differences. At 6.755 s, some slip starts to occur near the surface, at a time when there is no slip on the artificially created earthquake. Furthermore, the region of large slip in the artificially created earthquake is not observed in the inversion. Also, unlike the artificially created earthquake, no backward propagation of the rupture near the surface at about 7.315 s is found, although both rupture models have reached the surface by this time. Although the rupture is allowed to continue longer in the inversion, it actually stops at the correct time with respect to the artificially created earthquake.

This test shows that the inversion is capable of retrieving reliably the general features of the slip history. This is due to the fact that the ellipses recover the main characteristics of the rupture area. However, the test also shows that the two similar rupture history are the result of different stress conditions and frictional properties on the fault. It illustrates the nonuniqueness that is associated with the dynamic inversion. This is an issue that we will discuss in the following sections, in the case of a real earthquake, that is the Parkfield earthquake.

Two additional synthetic tests have also been carried out, each with a different source process. One ruptures a single horizontal patch with a rupture that propagates at about 3 km/s, and one with a more complicated rupture process which contains a jump of the rupture between one patch at the hypocenter and another located about 15 km away from it. Because those additional tests lead to similar conclusions as we have presented here, we do not discuss them further. They are discussed in detail by in the supporting information (see Text S1 and Figures S1–S6).

4. Dynamic Inversion of the 2004 Parkfield Earthquake

The results of the dynamic inversion using artificial data, discussed above, give us confidence that we can obtain a reliable dynamic rupture process for the Parkfield earthquake. We therefore carry out the full dynamic inversion.

The inversion of the three-component displacement seismograms reaches a misfit value of 0.29 (Figure 6), which is within the range of value obtained by *Twardzik et al.* [2012] for their kinematic inversions. The variations of the misfit value still observed at the end of the inversion are caused by small variations in the way that the different parameters combine together, since each parameter of the inversion has converged toward its final value (see Figure S7). This shows the high sensitivity of the dynamic modeling to the stress conditions and the frictional properties of the fault plane. The comparison between the calculated and the observed waveforms (Figure 7) shows that the main pulses are fitted in amplitude and phase for almost every traces. We also observe a better fit at stations located on the northeastern side of the fault compared to those on the southwestern side, which could be due to the fact that the velocity structure on the two sides of the fault are not the exactly the same.

Figure 8a shows the distribution of stress prior to the rupture and Figure 8b the distribution of material strength defined by the ellipses. Snapshots of the slip history for the lowest misfit rupture model are shown in Figure 8c. The rupture essentially breaks one major ellipse elongated in the strike direction. There is also a circular region, with smaller slip below the hypocenter. The rupture model reaches a final seismic moment

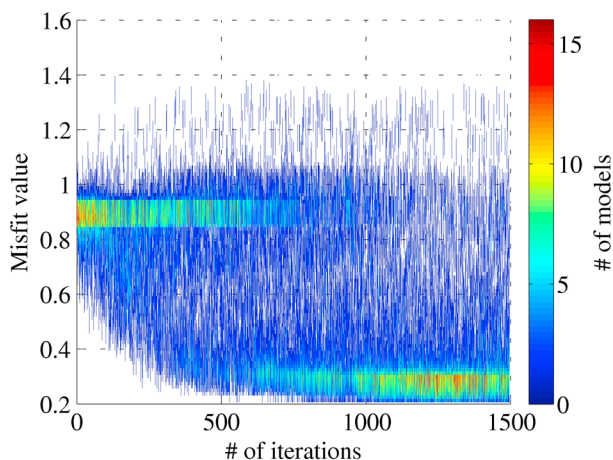


Figure 6. Evolution of the misfit with respect to the number of iterations. For each iteration, the misfit value range (0.2–1.6) is divided into bins of $[\epsilon - 0.0125 \epsilon + 0.0125]$, where ϵ is the central misfit value of the corresponding bin. Inside each bin, we count the number of models present. The red color corresponds to the bins with many models, while the blue color corresponds to the bins with only few models. Note that in Figure S7, we also show the convergence curve of each parameter of the inversion.

of 1.18×10^{18} N m, which is $\sim 4\%$ larger than the CMT value. We point out that the seismic moment was not constrained during the inversion and this close match is therefore reached by the inversion itself. From Figure 8c, we observe that the rupture terminates between ~ 7.3 and 7.9 s, well below the 11.2 s that is permitted. We find an average rupture speed of 2.8 km/s for the main ellipse, and there is little variation in this speed during the rupture process. The circular region near the hypocenter ruptures faster than the main ellipse with a speed of ~ 3.8 km/s, which is 10% higher than the shear wave speed at that depth. In the next section, we shall show that this circular region is not a robust feature of the rupture process. The entire dynamic rupture model is similar to that obtained by the kinematic inversion 1 of *Twardzik et al.* [2012]. Thus, using the same data

set, the two different approaches (kinematic and dynamic) have produced similar rupture models. When compared to the different solutions in Figure 1, the rupture model obtained from the fully dynamic inversion also shows good agreement with most models, and in particular, with the dynamic model obtained by *Ma et al.* [2008].

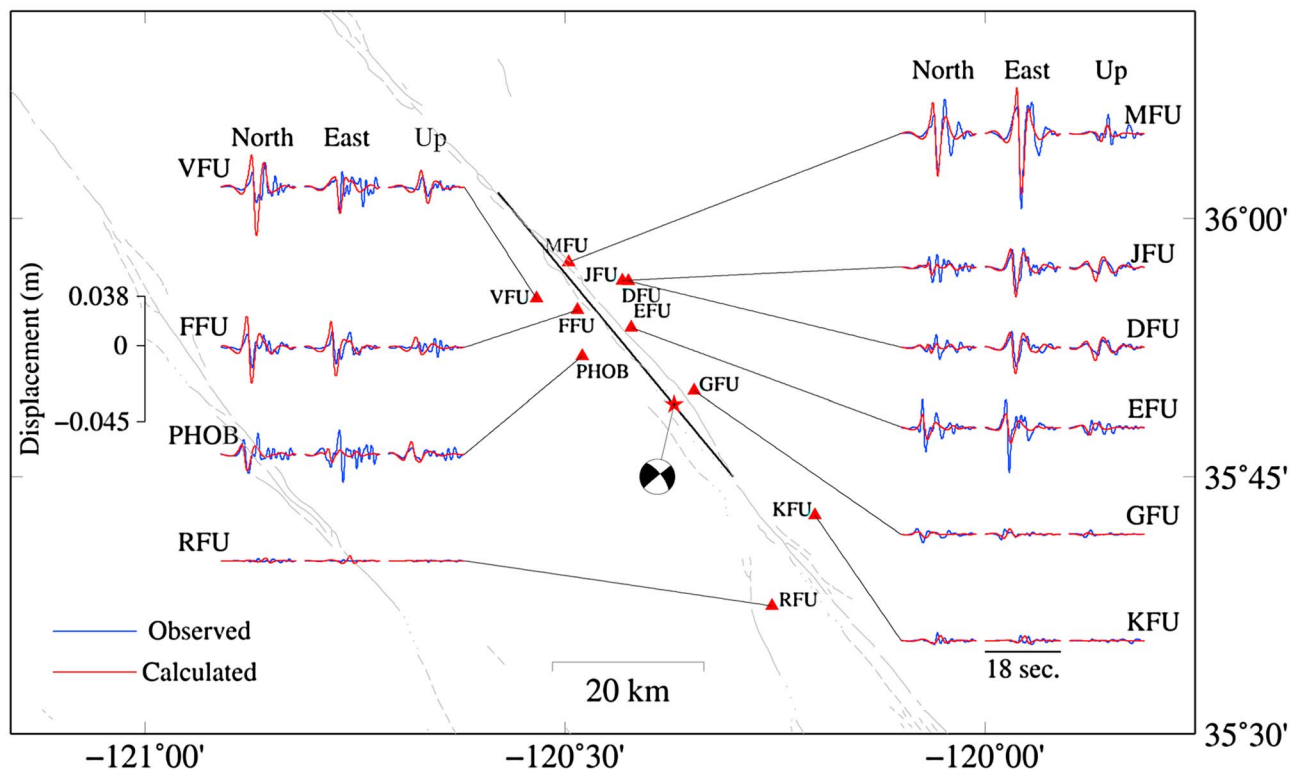


Figure 7. Comparison of the calculated seismograms from the lowest misfit rupture model obtained by the full dynamic inversion (red) and the observed data (blue). See caption of Figure 2 for further details.

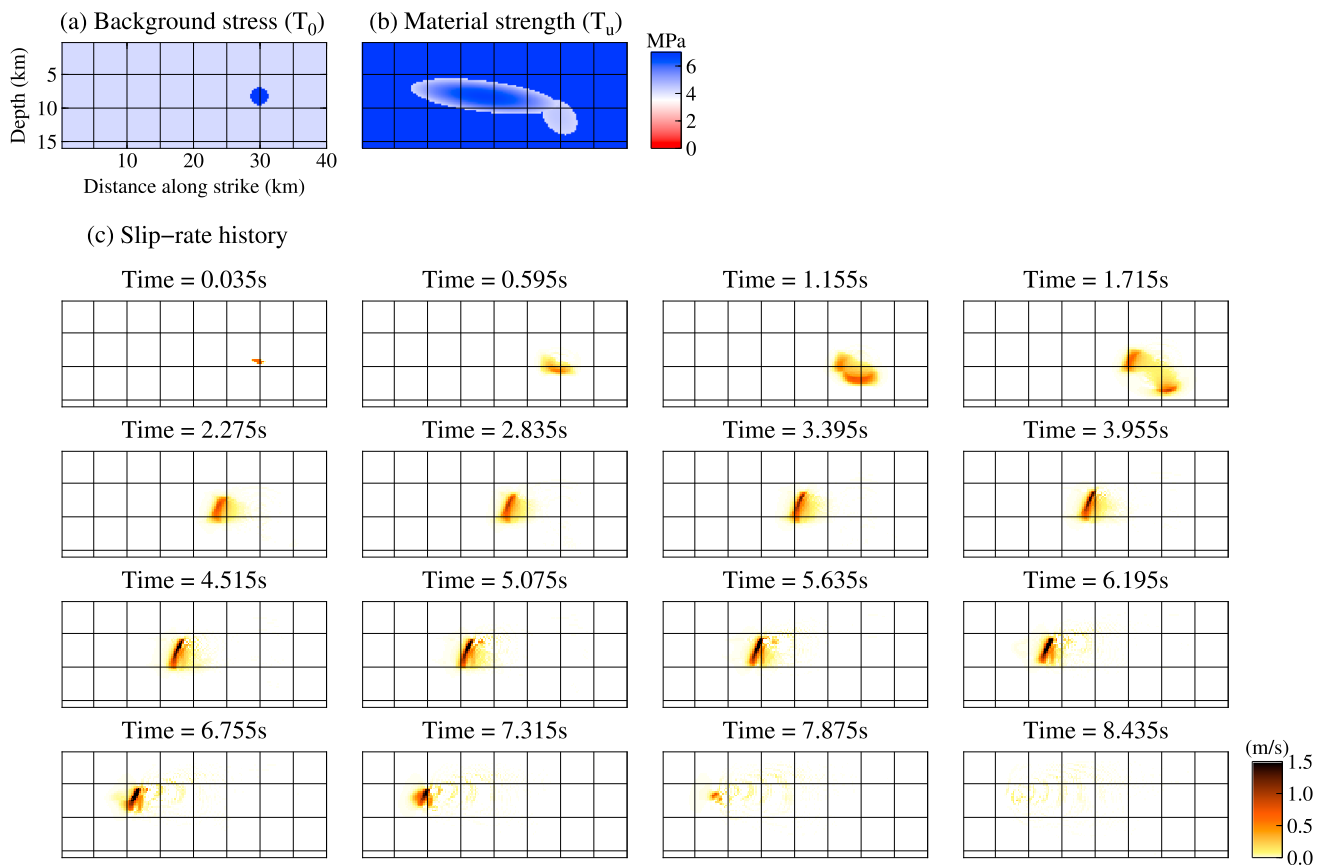


Figure 8. (a) Initial distribution of stress on the fault prior to rupture, obtained from the fully dynamic inversion. The initial circular patch necessary to trigger the rupture at the hypocenter is shown by the blue area. (b) Distribution of the material strength on the fault plane obtained from the inversion. Outside the ellipses, the material strength is set very high to avoid rupture there. (c) Snapshots of the resulting slip rate history from the stress and strength conditions of the lowest misfit model obtained by the full dynamic inversion. Each snapshot is separated from the next by a time step of 0.56 s.

The stress conditions and frictional properties obtained by the dynamic inversion are summarized in Figure 9, which shows the distribution of values explored during the inversion for the six dynamic parameters. We see that the circular region below the hypocenter is weak (S_1 of 0.08), while the main ellipse is stronger with an S_2 of 0.7, the difference between the two being manifested in the different rupture speeds observed for each. The stress drop (T_0) of the lowest misfit model is 4.2 MPa, which is an average of *Ma et al.* [2008]’s model, who find a stress drop of 10 MPa in the hypocentral region, with the remaining part of the fault having a stress drop of ~ 2 MPa. Our slip-weakening distance for the lowest misfit model is ~ 0.17 m, which is close to the chosen value of 0.15 m in *Ma et al.* [2008]. We find the energy release rate for the hypocentral circle to be $3.8 \times 10^5 \text{ J m}^{-2}$ and for the main ellipse to be $5.8 \times 10^5 \text{ J m}^{-2}$. This again is in good agreement with the dynamic model of *Ma et al.* [2008] as well as with values obtained from laboratory experiments and compilation of seismological estimates by *Nielsen et al.* [2013].

We compute the value of κ , the nondimensional parameter introduced by *Madariaga and Olsen* [2000], given by

$$\kappa = \frac{T_0^2 x_b}{\mu T_u D_c} \tag{7}$$

where μ is the average shear modulus. κ derives from the competition between a measure of the strain energy released during rupture and the energy dissipated in fracture. It is roughly the strain energy change per unit fault surface divided by the energy release rate and controls the characteristics of the rupture process. It defines a bifurcation at a critical value (κ_c), such that if $\kappa < \kappa_c$, the rupture does not grow, while if $\kappa > \kappa_c$, the rupture propagates at increasing speed as κ increases. From *Madariaga and Olsen* [2000], we can estimate κ_c to be around 1.09 for a flat circular crack. In this study, we obtain κ of about 2.0 for the

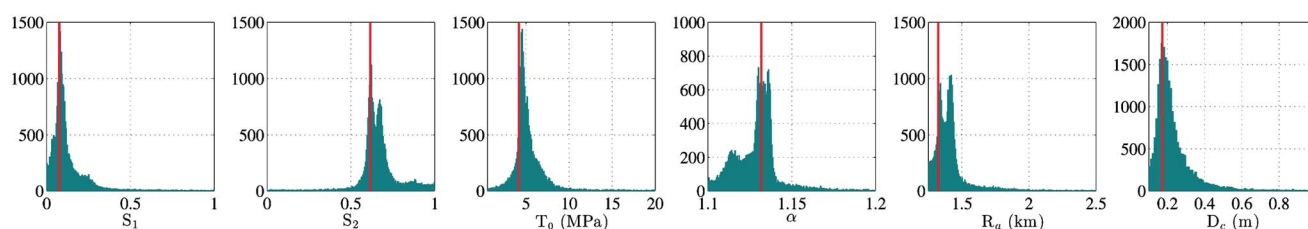


Figure 9. Each panel represents the distribution of values explored during the inversion for each inverted dynamic parameter. The first and second panels represent the distribution of the S value, S_1 referring to the ellipse that will converge below the hypocenter and S_2 referring to the ellipse that will become the major patch. The third panel represents the tectonic stress or stress drop (T_0). The fourth and fifth panels represent the strength ($T_a = \alpha T_{a_{\max}}$) and the size (R_a) of the initial circular patch. The last panel represents the slip-weakening distance of the friction law. The vertical lines show the optimal value for each parameter.

hypocentral circle (κ_1) and about 1.4 for the main ellipse (κ_2). κ_2 is very similar to the values obtained by others (e.g., 1.35–1.45 found by Ruiz and Madariaga [2013] in their study of the 2008 Iwate, Japan, earthquake). κ_1 is also in agreement with Ruiz and Madariaga [2013] and, as in their study, is associated with a supershear rupture speed.

We have also calculated R_c , which is the minimum size of the triggering rupture patch that is necessary for the rupture to grow. Because we use a initial circular patch, we determine R_c using the expression derived by Day [1982]:

$$R_c = \frac{7\pi T_a \mu}{24 T_0^2} D_c \quad (8)$$

For the lowest misfit model, we obtain $R_c \sim 1.7$ km. If we compute the ratio R_c/R_a , we obtain a value of about 1.3. To summarize, for the hypocentral circular patch, we have $S \sim 0.08$, $R_c/R_a \sim 1.3$ and a rupture speed of about the shear wave speed, and for the main ellipse, we have $S \sim 0.7$, $R_c/R_a \sim 1.3$ and a rupture speed of about the Rayleigh wave speed. These results agree with those of Andrews [1976] and Das and Aki [1977] when interpolated for a ratio R_c/R_a of about 1.0, R_c/R_a being equivalent to L_c/L in their relevant figures.

5. Exploration of the Dynamic Parameter Space

In order to efficiently explore the dynamic parameter space, we fix the geometry of the rupture area to that obtained by the fully dynamic inversion. This lowers the number of parameters from 16 to 6 and allows a broad investigation of the parameter space. The goal is to study the nonuniqueness associated with dynamic inversion. By looking at a large range of stress conditions and frictional properties of the fault, we can analyze under which conditions we can and cannot successfully fit the data. To perform this exploration, we use a Monte Carlo (MC) method [Metropolis and Ulam, 1949]. The MC method consists in generating random models inside the domain of parameter space that we want to explore. For each point in parameter space, we compute synthetic seismograms that are compared to the observed data. As explained by Tarantola [2005], the comparison between the observed and the predicted data defines whether a model is “acceptable” or not. Usually, the MC method is carried out until the parameter space has been sufficiently explored. In our case, we implemented MC exploration for $\sim 32,000$ randomly generated models. The range of values of the parameters used to generate the random models is summarized in Table 2. The reason we have to use the MC exploration is that the marginal probability density functions for the parameters are non-Gaussian so that the usual statistics based on standard deviation are incorrect [Tarantola, 2005].

The lowest misfit model found by the MC exploration has a misfit value of 0.30, which is essentially the same as the one reached by the dynamic inversion. There is consequently no visible differences between the calculated waveforms from the two rupture models. However, Table 2 shows that the MC exploration has found values for the dynamic parameters that are different than those found by the fully dynamic inversion. If we look at the details of the rupture process (Figure 10), we observe that the major difference is that the circular region below the hypocenter does not rupture. Since this does not affect significantly the calculated waveforms, it suggests that this patch may not be a robust feature. Therefore, we will focus only on the major ellipse from here on. The seismic moment is higher than the one obtained by the full dynamic inversion (1.42×10^{18} N m instead of 1.18×10^{18} N m), as is the average rupture speed of the main ellipse (3.3 km/s), but which is still below the shear wave speed of the medium at the depth range of the rupture.

Table 2. Range of Values Explored Using the Monte Carlo Method for Each of the Six Dynamic Parameters^a

Parameters ^b	S_1	S_2	T_0 (MPa)	α	R_a (km)	D_c (m)
Lower bound	0.00	0.00	0.50	1.10	1.25	0.10
Upper bound	1.00	1.00	20.00	1.20	2.50	2.00
Optimal value (Inv)	0.08	0.62	4.16	1.13	1.33	0.17
Optimal value (MC)	0.98	0.49	5.76	1.17	1.57	0.30

^aIt also shows the optimal value obtained by the Monte Carlo (MC) exploration and by the full dynamic inversion (Inv).

^b S_1 is S for the hypocentral circular region and S_2 that for the main ellipse.

If we only focus on the main ellipse, we can further reduce the parameter space from a 6-D space to a 5-D space ($S_2, T_0, D_c, R_a,$ and T_a). Since this is still not possible to visualize, we contract it into a space of lower dimension by computing the two nondimensional parameters κ and R_c/R_a for every model. Together with the third nondimensional parameter, that is S , we obtain a 3-D space containing the five parameters explored by the MC method. Figure 11 shows all the models sampled by the MC method projected within the 3-D space as well as the three different cross sections associated with it. The dots are color coded according to either the average rupture speed (Figure 11a) or the seismic moment (Figure 11b). We show with dots, outlined in black, the rupture models with $\epsilon \leq 0.35$ (ϵ given in equation (6)), which is an upper limit above which we consider that a rupture model does not fit the data reasonably well. From now on, these well fitting rupture models will be referred as LMMs (low misfit models). Figure 11 shows that the LMMs focus on a rather small region in the $(\kappa, R_c/R_a)$ plane, indicating that these two parameters strongly control the fit to the data. This implies that they control how strongly the rupture is triggered and how much energy comes in and goes out of the system during the propagation of the rupture. On the other hand, the LMMs spread

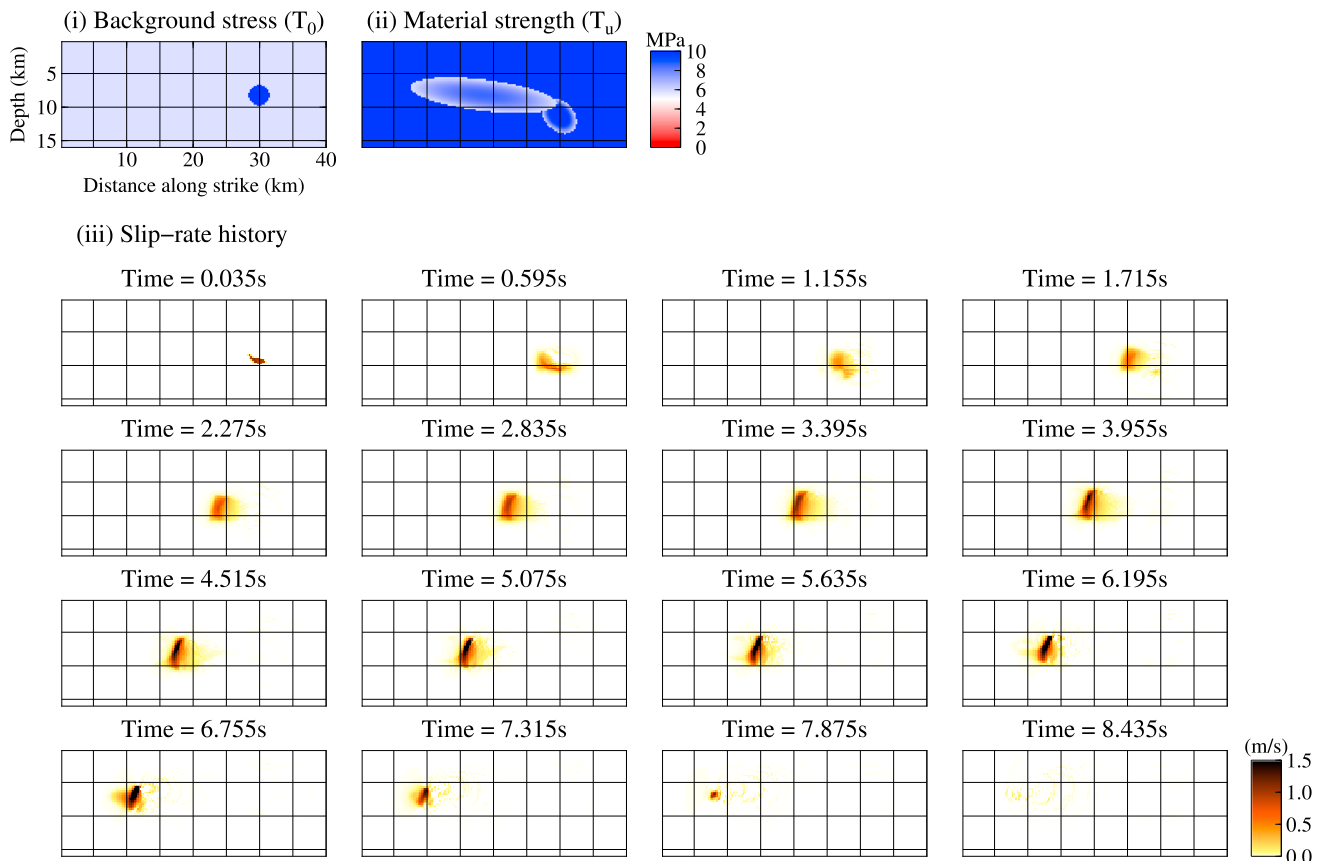


Figure 10. Same as Figure 8 but for the Monte Carlo exploration. Note that the color bar for the stress and strength has been slightly changed compared to Figure 8 in order to better show the results.

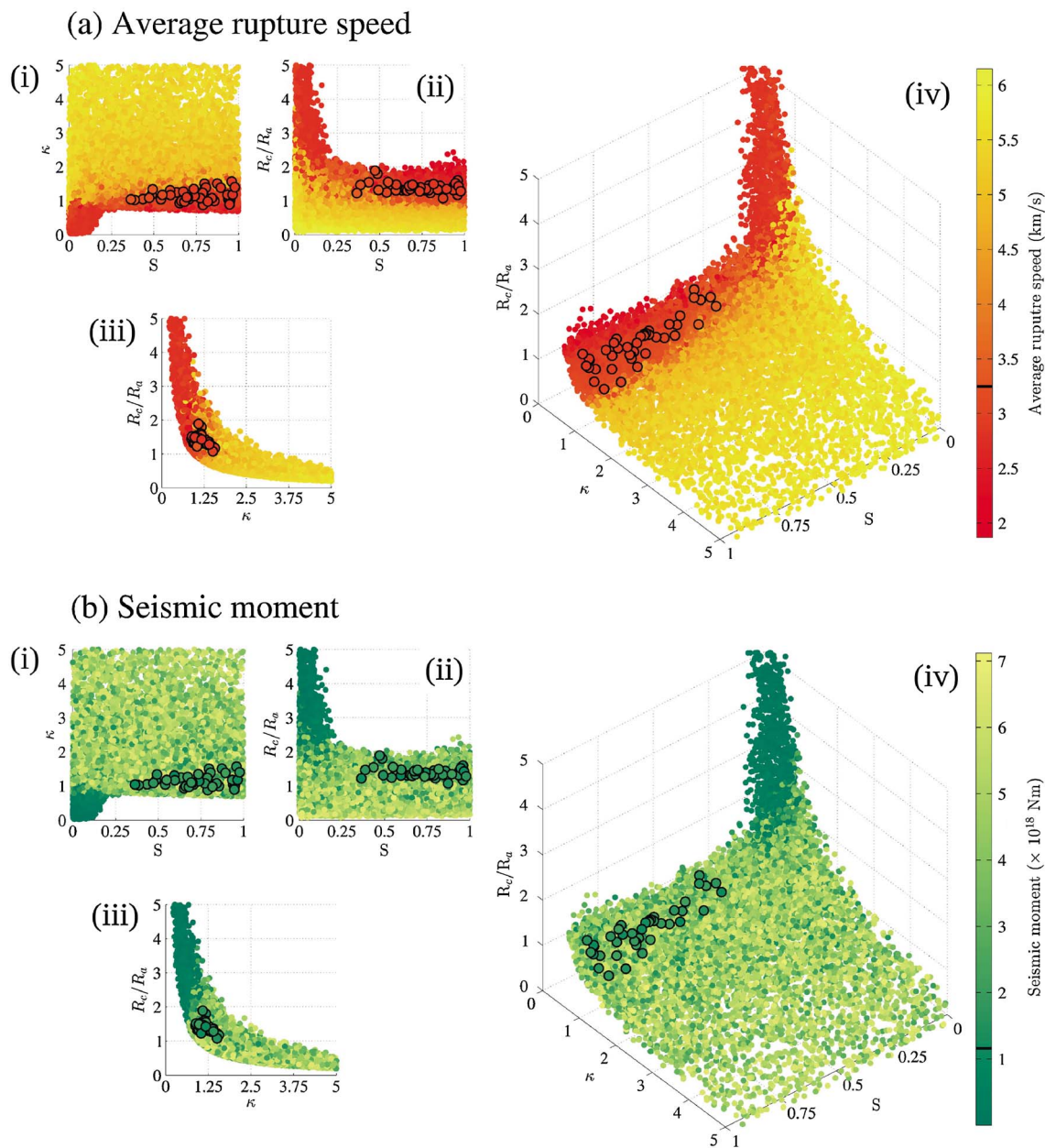


Figure 11. (a) Average rupture speed; (b) Seismic moment. (i) (S, κ) plane; (ii) $(S, R_c/R_a)$ plane; (iii) $(\kappa, R_c/R_a)$ plane; (iv) Projection of the rupture models sampled by the Monte Carlo method onto the 3-D space defined by S , κ , and R_c/R_a . In all subplots, the large dots represent rupture models associated to a misfit value ≤ 0.35 . In Figure 11a, the rupture models are color coded according to the average rupture speed. The black line on the color bar shows the value of the shear wave speed of the medium at the depth of the rupture. In Figure 11b, the rupture models are color coded according to the final seismic moment. The black line on the color bar shows the value of the seismic moment taken from GCMT.

over a large range of S values, showing that the seismic data used in this study do not constrain it well. Consequently, the strength of the elliptical patch does not play a major role as long as it is possible to break it. However, we can still put a lower bound on S of ~ 0.3 below which there are no LMMs.

The (κ, S) and $(R_c/R_a, S)$ planes in Figures 11a (i and ii) and 11b (i and ii) also show that except for $S < 0.1$, we have a threshold for κ and R_c/R_a . This threshold value for κ is ~ 0.6 , below which there is no propagating rupture and agrees well with theoretical predictions [Madariaga and Olsen, 2000]. The threshold value for R_c/R_a is ~ 2.0 , above which there is no propagating rupture. This is important because it shows that some regions of the parameter space can easily be ruled out by the Neighborhood Algorithm since they do not contain possible rupturing models. Figure 11a (i and ii) further shows that the LMMs are bounded on top or bottom by the transition from subshear to supershear rupture speed, clearly indicating that the best

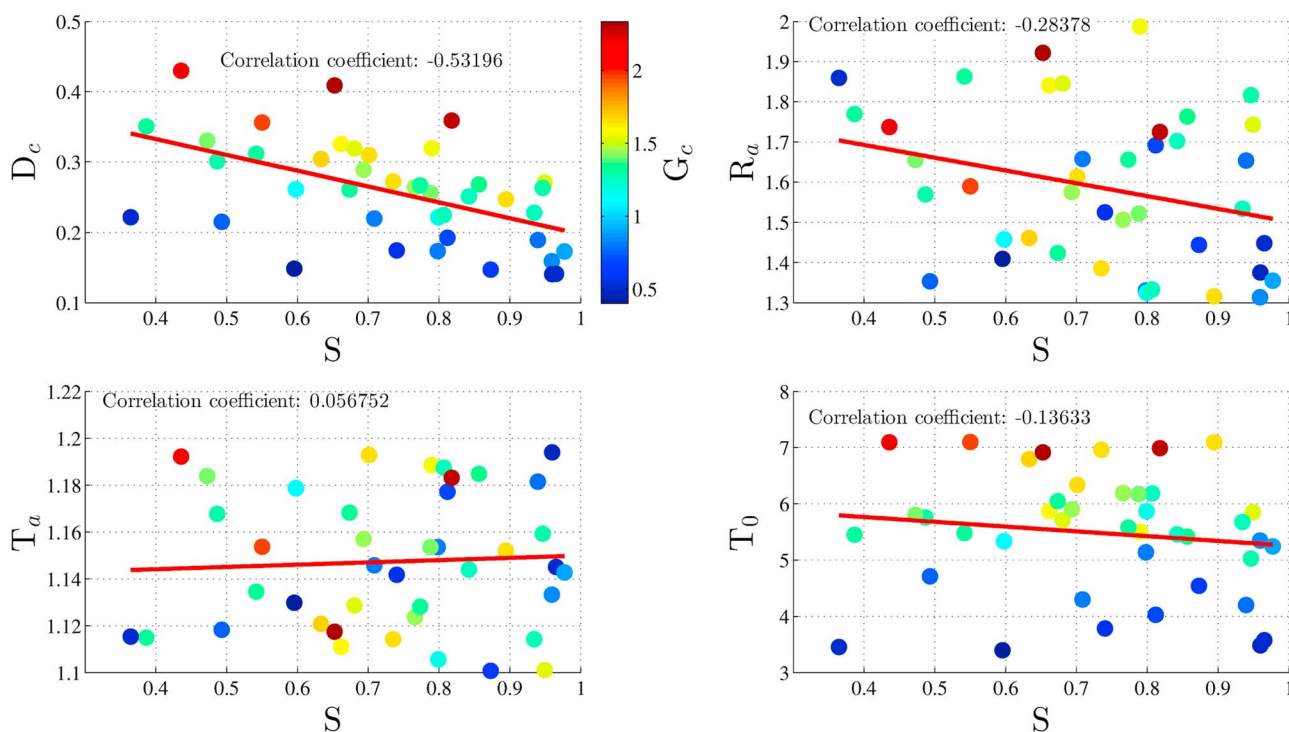


Figure 12. Correlation between S and the other dynamic parameters (D_c , R_a , and T_0) for the low misfit models. The dots are color coded according to the energy release rate (G_c). On each plot is shown the value of the correlation factor.

fitting rupture models are subshear. Figure 11b shows a lack of strong organization of the parameter space relative to the seismic moment, except for $S < 0.1$, $\kappa < 0.6$, and $R_c/R_a > 2.0$, where there is always propagation of the rupture at low rupture speed (< 2.5 km/s) and that reaches a low final seismic moment ($< 1.0 \times 10^{18}$ N m). The chaotic structure of the parameter space relative to the seismic moment shows that the dynamic parameters essentially control the rupture speed. However, despite the disorder, the LMMs all have a seismic moment close to the GCMT value, showing that this is also an important feature of a rupture model if one wants to fit waveform data.

We have done a detailed investigation of the rupture process for each of the LMMs (see Figure S8). We observe that despite the fact that the LMMs span a broad range of S values ($0.3 < S < 1.0$), they all produce very similar rupture processes with subshear rupture speed. Andrews [1976] and Das and Aki [1977] showed that the domain of subshear rupture speed extends over a wide range of value for S , and because a subshear rupture speed is required to fit the data correctly, it explains the lack of constraints on S . We also observe that the smaller S is, the wider the rupture front is. We computed the correlation coefficient between S and D_c , as well as between S and the other dynamic parameters (T_0 , R_a , and T_a). Figure 12 shows that for the last three parameters, there is no noticeable correlation. On the other hand, S and D_c show a weak correlation, illustrating the trade-off between S and D_c [e.g., Guatteri and Spudich, 2000; Goto and Sawada, 2010]. This trade-off appears because the fracture energy is very similar for different LMMs. This enhances the nonuniqueness of dynamic inversion, requiring a careful examination of the parameter space as argued by Corish et al. [2007].

6. Conclusion

We have performed a fully dynamic inversion for the rupture process of the 28 September 2004, M_w 6.0, Parkfield earthquake using a method in which stress and frictional properties on the fault are described by ellipses. Synthetic tests validate the fact that it is possible to reliably recover the rupture history of an earthquake using the method of elliptical subfaults approximation. However, we find that determining the stress conditions and frictional properties on the fault is more difficult.

To summarize, the source process of this earthquake can be essentially described by one ellipse, 22 km long and 4 km wide, elongated along strike, within which the rupture occurs at a nearly constant speed of ~ 2.8 km/s and with a seismic moment of 1.2×10^{18} N m. When compared to all the different solutions obtained for this earthquake, we observe that our source process falls within the range of models found by others. To investigate the variability of plausible rupture models, we have explored the dynamic parameter space, fixing the geometry of the rupture area from that found by the inversion, using a Monte Carlo method. We observe that we can obtain a plausible rupture model if $0.3 < S < 1.0$. We also observe that there is an optimal combination of the two physical parameters, κ and R_c/R_g , defining a narrow region inside the parameter space where all the plausible rupture models lie, showing that these strongly control the fit to the data. Similar conclusions were reached by *Nielsen and Olsen* [2000] in the course of the study of the 1994 M_w 6.7 Northridge earthquake. They showed that only certain combinations of the initial conditions and friction on the fault are able to produce a rupture model that fits the data. In our case, the MC method allowed us to do a broader exploration of the plausible rupture models in order to support these conclusions.

The fully dynamic inversion can therefore provide a range of plausible stress conditions and frictional properties on the fault and also constrains the rupture speed well. Incorporating other kinds of data into the inversion may help to obtain further details of the stress and frictional properties on the fault.

Acknowledgments

Research by C.T. was supported by QUEST, funded under the EC Marie Curie Initial Training Network grant agreement 238007. Partial support was provided through grant ANR-2011-BS56-017 of the French "Agence Nationale de la Recherche." We thank the GEOS network for the use of their data. The data for this paper are available at the Strong-Motion Virtual Data Center (VDC). Data set: <http://www.strongmotioncenter.org/vdc/scripts/event.plx?evt=941>. We also thank Javier Ruiz for providing the k^2 -type slip distributions.

References

- Andrews, D. J. (1976), Rupture velocity of plane strain shear cracks, *J. Geophys. Res.*, *81*(32), 5679–5687, doi:10.1029/JB081i032p05679.
- Archuleta, R. J. (1984), A faulting model for the 1979 Imperial Valley earthquake, *J. Geophys. Res.*, *89*(B6), 4559–4585, doi:10.1029/JB089iB06p04559.
- Barnhart, W. D., and R. B. Lohman (2010), Automated fault model discretization for inversions for co-seismic slip distributions, *J. Geophys. Res.*, *115*, B10419, doi:10.1029/2010JB007545.
- Bennington, N., C. Thurber, K. L. Feigl, and J. Murray-Moraleda (2011), Aftershock distribution as a constraint on the geodetic model of co-seismic slip for the 2004 Parkfield earthquake, *Pure Appl. Geophys.*, *168*, 1553–1565, doi:10.1007/s00024-010-0214-x.
- Borcherdt, R. D., J. B. Fletcher, E. G. Jensen, G. L. Maxwell, J. R. VanSchaak, R. E. Warrick, E. Cranswick, M. J. S. Johnston, and R. McClearn (1985), A general earthquake observation system (GEOS), *Bull. Seismol. Soc. Am.*, *71*(4), 959–971.
- Bouchon, M., H. Sekiguchi, K. Irikura, and T. Iwata (1998), Some characteristics of the stress field of the 1995 Hyogo-ken Nanbu (Kobe) earthquake, *J. Geophys. Res.*, *103*(B10), 24,271–24,282, doi:10.1029/98JB02136.
- Bouchon, M., M. Nafi Toksöz, H. Karabulut, M. P. Boin, M. Dietrich, M. Aktar, and M. Edie (2002), Space and time evolution of rupture and faulting during the 1999 Izmit (Turkey) earthquake, *Bull. Seismol. Soc. Am.*, *92*(1), 256–266.
- Causse, M., L. A. Dalguer, and P. M. Mai (2014), Variability of dynamic source parameters inferred from kinematic models of past earthquakes, *Geophys. J. Int.*, *196*(3), 1754–1769, doi:10.1093/gji/ggt478.
- Clayton, R., and B. Engquist (1977), Absorbing boundary conditions for acoustic and elastic wave equations, *Bull. Seismol. Soc. Am.*, *67*(6), 1529–1540.
- Cohee, B. P., and G. C. Beroza (1994), Slip distribution of the 1992 Landers earthquake and its implications for earthquake source mechanics, *Bull. Seismol. Soc. Am.*, *84*(3), 692–712.
- Corish, S. M., C. R. Bradley, and K. B. Olsen (2007), Assessment of a nonlinear dynamic rupture inversion technique applied to a synthetic earthquake, *Bull. Seismol. Soc. Am.*, *97*(3), 901–914, doi:10.1785/0120060066.
- Cotton, F., and M. Campillo (1995), Frequency domain inversion of strong motions: Applications to the 1992 Landers earthquake, *J. Geophys. Res.*, *100*(B3), 3961–3975, doi:10.1029/94JB02121.
- Cotton, F., and O. Coutant (1997), Dynamic stress variations due to shear faults in a plane-layered medium, *Geophys. J. Int.*, *128*(3), 676–688, doi:10.1111/j.1365-246X.1997.tb05328.x.
- Cruz-Atienza, V. M., K. B. Olsen, and L. A. Dalguer (2009), Estimation of the breakdown slip from strong-motion seismograms: Insights from numerical experiments, *Bull. Seismol. Soc. Am.*, *99*(6), 3454–3469, doi:10.1785/0120080330.
- Custodio, S., M. T. Page, and R. J. Archuleta (2009), Constraining earthquake source inversion with GPS data: 2. A two-step approach to combine seismic and geodetic data sets, *J. Geophys. Res.*, *114*, B01315, doi:10.1029/2008JB005746.
- Dalguer, L. A., and S. M. Day (2007), Staggered-grid split-node method for spontaneous rupture simulation, *J. Geophys. Res.*, *112*, B02302, doi:10.1029/2006JB004467.
- Das, S., and K. Aki (1977), A numerical study of two-dimensional spontaneous rupture propagation, *Geophys. J. R. Astron. Soc.*, *50*(3), 643–668, doi:10.1111/j.1365-246X.1977.tb01339.x.
- Das, S., and B. V. Kostrov (1983), Breaking of a single asperity: Rupture process and seismic radiation, *J. Geophys. Res.*, *88*(B5), 4277–4288, doi:10.1029/JB088iB05p04277.
- Day, S. (1982), Three-dimensional simulation of spontaneous rupture: The effect of nonuniform pre-stress, *Bull. Seismol. Soc. Am.*, *72*(6A), 1881–1902.
- Delouis, B., D. Giardini, P. Lundgren, and J. Salichon (2002), Joint inversion of InSAR, GPS, teleseismic, and strong-motion data for the spatial and temporal distribution of earthquake slip: Application to the 1999 Izmit mainshock, *Bull. Seismol. Soc. Am.*, *92*(1), 278–299.
- Di Carli, S., C. Francois-Holden, S. Peyrat, and R. Madariaga (2010), Dynamic inversion of the 2000 Tottori earthquake based on elliptical sub-fault approximations, *J. Geophys. Res.*, *115*, B12238, doi:10.1029/2009JB006358.
- Fukuyama, E. (1991), Analysis and interpretation of the heterogeneous rupture process: Application of the empirical Green's function method and nonlinear inversion technique to large earthquake, *Tectonophysics*, *197*, 1–17, doi:10.1016/0040-1951(91)90396-A.
- Fukuyama, E., and T. Mikumo (1993), Dynamic rupture analysis: Inversion for the source process of the 1990 Izu-Oshima, Japan, earthquake ($M=6.5$), *J. Geophys. Res.*, *98*(B4), 6529–6542, doi:10.1029/92JB02451.
- Fukuyama, E., and T. Mikumo (2007), Slip-weakening distance estimated at near-fault stations, *Geophys. Res. Lett.*, *34*, L09302, doi:10.1029/2006GL029203.

- Goto, H., and S. Sawada (2010), Trade-offs among dynamic parameters inferred from results of dynamic source inversion, *Bull. Seismol. Soc. Am.*, *100*(3), 910–922, doi:10.1785/0120080250.
- Guatteri, M., and P. Spudich (2000), What can strong-motion tell us about slip-weakening fault-friction law?, *Bull. Seismol. Soc. Am.*, *90*(1), 98–116.
- Guo, Y., K. Koketsu, and T. Ohno (2013), Analysis of the rupture process of the 1995 Kobe earthquake using a 3D velocity structure, *Earth Planets Space*, *65*(12), 1581–1586, doi:10.5047/eps.2013.07.006.
- Hamano, Y. (1974), Dependence of rupture time history on the heterogeneous distribution of stress and strength on the fault plane (abstract), *Eos Trans. AGU*, *55*, 352.
- Hernandez, B., F. Cotton, and M. Campillo (1999), Contribution of radar interferometry to a two-step inversion of the kinematic process of the 1992 Landers earthquake, *J. Geophys. Res.*, *104*(B6), 13,083–13,099, doi:10.1029/1999JB900078.
- Houlié, N., D. Dreger, and A. Kim (2013), GPS source solution of the 2004 Parkfield earthquake, *Sci. Rep.*, *4*(3646), 1–9, doi:10.1038/srep03646.
- Iida, Y. (1972), Cohesive force across the tip of a longitudinal-shear crack and Griffith's specific surface energy, *J. Geophys. Res.*, *77*(20), 3796–3805, doi:10.1029/JB077i020p03796.
- Ide, S., and M. Takeo (1997), Determination of constitutive relations of fault slip based on seismic wave analysis, *J. Geophys. Res.*, *102*(B12), 27,379–27,391, doi:10.1029/97JB02675.
- Jennings, C. W. (1994), Fault activity map of California and adjacent areas, *Geologic Data Map 6*, scale 1:750,000, Dept. of Conserv., Div. of Mines and Geol., Sacramento, Calif.
- Johanson, I. A., E. J. Fielding, F. Rolandone, and R. Bürgmann (2006), Co-seismic and post-seismic slip of the 2004 Parkfield earthquake from Space-Geodetic Data, *Bull. Seismol. Soc. Am.*, *96*(4B), 269–282, doi:10.1785/0120050818.
- Kim, A., and D. S. Dreger (2008), Rupture process of the 2004 Parkfield earthquake from near-fault seismic waveform and geodetic records, *J. Geophys. Res.*, *113*, B07308, doi:10.1029/2007JB005115.
- Koketsu, K., S. Yoshida, and H. Higashihara (1998), A fault model of the 1995 Kobe earthquake derived from the GPS data on the Akashi Kaikyo bridge and other datasets, *Earth Planets Space*, *50*(10), 803–811.
- Liu, P., S. Custodio, and R. J. Archuleta (2006), Kinematic inversion of the 2004 M_w 6.0 Parkfield earthquake including an approximation to site effects, *Bull. Seismol. Soc. Am.*, *96*(4B), 143–158, doi:10.1785/0120050826.
- Liu, P., S. Custodio, and R. J. Archuleta (2008), Erratum to Kinematic inversion of the 2004 M_w 6.0 Parkfield earthquake including an approximation to site effects, *Bull. Seismol. Soc. Am.*, *98*(4), 2101, doi:10.1785/0120080959.
- Ma, S., S. Custodio, R. J. Archuleta, and P. Liu (2008), Dynamic modelling of the 2004 M_w 6.0 Parkfield, California earthquake, *J. Geophys. Res.*, *113*, B02301, doi:10.1029/2007JB005216.
- Madariaga, R. (1979), On the relation between seismic moment and stress drop in the presence of stress and strength heterogeneity, *J. Geophys. Res.*, *84*(B5), 2243–2250, doi:10.1029/JB084iB05p02243.
- Madariaga, R., and K. B. Olsen (2000), Criticality of rupture dynamics in 3D, *Pure Appl. Geophys.*, *157*(11–12), 1981–2001, doi:10.1007/PL00001071.
- Madariaga, R., K. B. Olsen, and R. J. Archuleta (1998), Modelling dynamic rupture in a 3D earthquake fault model, *Bull. Seismol. Soc. Am.*, *88*(5), 1182–1197.
- Mendoza, C., and S. Hartzell (2008), Finite-fault analysis of the 2004 Parkfield, California, earthquake, using P_{nl} waveforms, *Bull. Seismol. Soc. Am.*, *98*(6), 2746–2755, doi:10.1785/0120080111.
- Metropolis, N., and S. Ulam (1949), The Monte Carlo method, *J. Am. Stat. Assoc.*, *44*(247), 335–341, doi:10.1080/01621459.1949.10483310.
- Mikumo, T., K. Hirahara, and T. Miyatake (1987), Dynamical fault rupture processes in heterogeneous media, *Tectonophysics*, *144*, 19–36, doi:10.1016/0040-1951(87)90006-0.
- Mikumo, T., K. B. Olsen, E. Fukuyama, and Y. Yagi (2003), Stress-breakdown time and slip-weakening distance inferred from slip-velocity functions on earthquake faults, *Bull. Seismol. Soc. Am.*, *93*(1), 264–282, doi:10.1785/0120020082.
- Murray, J., and J. Langbein (2006), Slip on the San Andreas fault at Parkfield, California, over two earthquake cycles and the implications for seismic hazard, *Bull. Seismol. Soc. Am.*, *96*(4B), 283–303, doi:10.1785/01120050820.
- Nielsen, S. B., and K. B. Olsen (2000), Constraints on stress and friction from dynamic rupture models of the 1994 Northridge, California, earthquake, *Pure Appl. Geophys.*, *157*(11–12), 2029–2046, doi:10.1007/PL00001073.
- Nielsen, S., E. Spagnuolo, V. Violay, S. Smith, P. Scarlato, G. Romeo, F. Di Felice, and G. Di Toro (2013), Measuring fracture energy under co-seismic conditions (abstract), *EGU*, *15*, id. EGU2013-11045.
- Peyrat, S., and K. B. Olsen (2004), Nonlinear dynamic rupture inversion of the 2000 Western Tottori, Japan, earthquake, *Geophys. Res. Lett.*, *31*, L05604, doi:10.1029/2003GL019058.
- Peyrat, S., K. B. Olsen, and R. Madariaga (2001), Dynamic modelling of the 1992 Landers earthquake, *J. Geophys. Res.*, *106*(B11), 26,467–26,482, doi:10.1029/2001JB000205.
- Peyrat, S., K. B. Olsen, and R. Madariaga (2004), Which dynamic rupture parameters can be estimated from strong ground motion and geodetic data?, *Pure Appl. Geophys.*, *161*, 2155–2169, doi:10.1007/s00024-004-2555-9.
- Pulido, N., and K. Irikura (2000), Estimation of dynamic rupture parameters from the radiated seismic energy and apparent stress, *Geophys. Res. Lett.*, *27*(23), 3945–3948, doi:10.1029/2000GL011658.
- Quin, H. (1990), Dynamic stress drop and rupture dynamics of the October 15, 1979 Imperial Valley, California, earthquake, *Tectonophysics*, *175*(1–3), 93–117, doi:10.1016/0040-1951(90)90132-R.
- Ripperger, J., and P. M. Mai (2004), Fast computation of static stress changes on 2D faults from final slip distributions, *Geophys. Res. Lett.*, *31*, L18610, doi:10.1029/2004GL020594.
- Ruiz, J., D. Beaumont, P. Bernard, and C. Berge-Thierry (2007), New approach in the kinematic k^{-2} source model for generating physical slip velocity functions, *Geophys. J. Int.*, *171*, 739–754, doi:10.1111/j.1365-246X.2007.03503.x.
- Ruiz, S., and R. Madariaga (2011), Determination of the friction law parameters of the M_w 6.7 Michilla earthquake in northern Chile by dynamic inversion, *Geophys. Res. Lett.*, *38*, L09317, doi:10.1029/2011GL047147.
- Ruiz, S., and R. Madariaga (2013), Kinematic and dynamic inversion of the 2008 northern Iwate earthquake, *Bull. Seismol. Soc. Am.*, *103*(2A), 694–708, doi:10.1785/0120120056.
- Sambridge, M. (1999a), Geophysical inversion with a neighbourhood algorithm—I. Searching a parameter space, *Geophys. J. Int.*, *138*(2), 479–494, doi:10.1046/j.1365-246X.1999.00876.x.
- Sambridge, M. (1999b), Geophysical inversion with a neighbourhood algorithm—II. Appraising the ensemble, *Geophys. J. Int.*, *138*(2), 727–746, doi:10.1046/j.1365-246X.1999.00900.x.
- Sekiguchi, H., and T. Iwata (2002), Rupture process of the 1999 Kocaeli, Turkey, earthquake estimated from strong-motion waveforms, *Bull. Seismol. Soc. Am.*, *92*(1), 300–311.

- Spudich, P., and D. P. Miller (1990), Seismic site effects and the spatial interpolation of earthquake seismograms: Results using aftershocks of the 1986 North Palm Springs, California, earthquake, *Bull. Seismol. Soc. Am.*, *80*(6A), 1504–1532.
- Tarantola, A. (2005), *Inverse Problem Theory and Methods for Model Parameter Estimation*, Society for Industrial and Applied Mathematics, Philadelphia, Pa.
- Thurber, C., S. Roecker, K. Roberts, M. Gold, L. Powell, and K. Rittger (2003), Earthquake locations and three-dimensional fault zone structure along the creeping section of the San Andreas Fault near Parkfield, CA: Preparing for SAFOD, *Geophys. Res. Lett.*, *30*(3), 1112, doi:10.1029/2002GL016004.
- Twardzik, C., R. Madariaga, S. Das, and S. Custodio (2012), Robust features of the source process for the 2004 Parkfield, California, earthquake from strong-motion seismograms, *Geophys. J. Int.*, *191*(3), 1245–1254, doi:10.1111/j.1365-246X.2012.05653.x.
- Vallée, M., and M. Bouchon (2004), Imaging co-seismic rupture in far field by slip patches, *Geophys. J. Int.*, *156*(3), 615–630, doi:10.1111/j.1365-246X.2004.02158.x.
- Wald, D. J., and T. H. Heaton (1994), Spatial and temporal distribution of slip for the 1992 Landers, California, earthquake, *Bull. Seismol. Soc. Am.*, *84*(3), 668–691.
- Yagi, Y., and M. Kikuchi (2000), Source process of the Kocaeli, Turkey, earthquake of August 17, 1999, obtained by joint inversion of near-field data and teleseismic data, *Geophys. Res. Lett.*, *27*(13), 1969–1972, doi:10.1029/1999GL011208.
- Ziv, A. (2012), Inference of co-seismic slip via joint inversion of GPS and aftershock data: The 2004 Parkfield example, *J. Geophys. Res.*, *117*, B03307, doi:10.1029/2011JB008400.